nature COMMUNICATIONS

ARTICLE

https://doi.org/10.1038/s41467-020-16860-y OPEN

Understanding rate effects in injection-induced earthquakes

Maryam Alghannam[1] & Ruben Juanes[1✉]

Understanding the physical mechanisms that underpin the link between fluid injection and seismicity is essential in efforts to mitigate the seismic risk associated with subsurface technologies. To that end, here we develop a poroelastic model of earthquake nucleation based on rate-and-state friction in the manner of spring–sliders, and analyze conditions for the emergence of stick-slip frictional instability—the mechanism for earthquakes—by carrying out a linear stability analysis and nonlinear simulations. We find that the likelihood of triggering earthquakes depends largely on the rate of increase in pore pressure rather than its magnitude. Consequently, fluid injection at constant rate acts in the direction of triggering seismic rupture at early times followed by aseismic creep at late times. Our model implies that, for the same cumulative volume of injected fluid, an abrupt high-rate injection protocol is likely to increase the seismic risk whereas a gradual step-up protocol is likely to decrease it.

[1] Massachusetts Institute of Technology, 77 Massachusetts Ave, Cambridge, MA 02139, USA. ✉email: juanes@mit.edu

Subsurface fluid-injection operations have been recognized to carry a risk of inducing earthquakes since the 1960s[1]. While most of the injection-induced earthquakes are micro-tremors, they can occasionally be of large magnitude, such as the Prague M_w 5.7 earthquake in 2011[2], the Pawnee M_w 5.8 earthquake in 2016[3], and the Pohang M_w 5.5 earthquake in 2017[4], among others. The occurrence of induced earthquakes of large magnitude has motivated development of different operational strategies for seismic hazard mitigation. In particular, an early attempt to control seismicity at the Rangely oil field suggested maintaining the magnitude of fluid pressure below a critical threshold[5], based on a Coulomb failure model that links the magnitude of fluid pressure to the occurrence of induced earthquakes[6]. This model, however, does not address the evolution of the rupture and whether a fault slips seismically or aseismically. It was also insufficient to explain seismicity at Cogdell oil field, for instance, where earthquakes were observed in regions of low rather than high fluid pressure[7]. A different strategy to control seismicity involved maintaining the cumulative volume of injected fluid below a critical threshold[8], based on empirical observations and modeling linking the cumulative volume of injected fluid to the maximum magnitude of induced earthquakes[9]. This model, however, is at odds with the 2017 Pohang earthquake, as its magnitude exceeded the size estimated from the injected volume by 500 times[10].

A growing number of field observations suggests that managing fluid injection rates may be a promising tool to mitigate the occurrence of induced earthquakes. It is observed that low-rate wells, for instance, are much less likely to be associated with earthquakes than high-rate wells, and that the critical rate above which earthquakes are induced is likely dependent on reservoir properties[11,12]. It is also observed that temporal variation in injection rates is generally correlated with the frequency of earthquakes[1,13–15], and that abrupt increases in injection rates tend to shortly precede the occurrence of earthquakes[16–18]. While attempts have been made to explain some of these observations with seismicity-rate models[19–21] and 2D numerical simulations of coupled flow-geomechanics[22,23], the physical mechanisms behind the link between the rate of fluid injection and the occurrence of induced earthquakes remain poorly understood.

Seismicity-rate models based on the triggering-front concept consider the large-scale spatiotemporal effects of nonlinear diffusion on the probability of a given magnitude earthquake using Gutenberg–Richter statistics[24], but do not address the dynamics of the rupture and, in particular, whether a fault slips seismically or aseismically. Characterizing fault slip mode is essential to mitigate the seismic risk associated with subsurface operations, as it has been observed that an increase in pore pressure magnitude leads to seismic slip in some sites[1–5,25] and aseismic slip in others[7,26–30]. Here we develop a poroelastic model of induced earthquake nucleation in the manner of spring–sliders[31–35] based on rate-and-state friction[32,36], and we study the effect of injection rate on stick-slip frictional behavior—the mechanism for seismic slip[37].

Our model shows that the likelihood of triggering earthquakes depends critically on the rate of increase in pore pressure. We find that fluid injection at constant rate acts in the direction of triggering seismic rupture at early times followed by aseismic creep at late times. This finding is qualitatively consistent with laboratory observations of sliding between saturated rocks at both transient and steady-state pore pressure conditions[38–40], and may explain field observations of triggered and induced seismicity from subsurface operations in different geologic settings[1,11–14,16–18].

Results and discussion

Poroelastic spring–slider model. When fluid is injected into a faulted reservoir, the pore pressure change induces effective stress variations in the reservoir and surrounding rock (Fig. 1a). To model the effects of variations in effective normal stress on a creeping fault segment, we develop a poroelastic spring–slider model of frictional slip (Fig. 1b). Our model consists of a slider of unit base area that is pulled by a spring whose end is constrained to move at a steady slip rate. The spring stiffness accounts for the elastic interaction of the sliding surface with the surrounding rock. The slider represents the injection-driven deformation process, where a piston is loaded vertically and compresses a spring inside a fluid-filled space. The vertical spring is analogous to the rock skeleton, while the fluid inside the slider represents fluid in the rock pores subject to increase from fluid injection and decrease from pressure diffusion. Our model accounts for the poroelastic coupling between the shear and effective normal stresses along the fault.

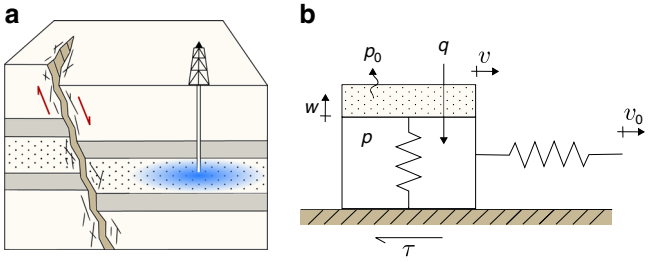

Fig. 1 Conceptual picture of induced seismicity including poroelastic effects. a Fluid injection induces effective stress changes in the reservoir surrounding the fault, increasing the likelihood of fault slip and earthquake triggering. **b** Our spring-poroslider model of a fault segment in contact with the reservoir. Here, v_0 is the loading velocity, v is the velocity of the block, τ is the frictional shear force, w is the elongation of the piston, q is the injection rate, p_0 is the ambient pressure, and p is the pressure inside the slider.

Frictional evolution is modeled by the rate-and-state constitutive laws[32,36], which are capable of reproducing a wide range of observed seismic and aseismic fault behaviors ranging from preseismic slip and earthquake nucleation to coseismic rupture and earthquake afterslip[41]. These laws propose that the frictional shear stress is a function of the effective normal stress and a coefficient of friction that is dependent on slip rate and the state of the sliding surface. Since the effective normal stress varies as a result of fluid injection, we adopt Linker and Dieterich's[42] formulation for the coefficient of friction and couple it with a poroelastic model of pore pressure and rock deformation. We derive the poroelastic model from the principles of mass and momentum conservation, and find that pore pressure satisfies a diffusion equation that leads to transient behavior at early times and steady-state behavior at late times.

The dimensional equations describing the dynamic motion of the poroelastic spring–slider system with an evolving pore pressure take the form (see Supplementary Note 1 for the derivation of the equations):

$$\dot{U} = V_0 - V, \tag{1}$$

$$\dot{V} = \frac{1}{(T/2\pi)^2}\left[U - \frac{1}{k_s}\left(\mu_* + \hat{a}\ln\frac{V}{V_*} + \Theta\right)(\Sigma - P)\right], \tag{2}$$

$$\dot{\Theta} = -\frac{V}{d_c}\left(\Theta + \hat{b}\ln\frac{V}{V_*}\right) + \hat{\alpha}\frac{\dot{P}}{(\Sigma - P)}, \tag{3}$$

$$\dot{P} = \frac{k_n^{\mathrm{eff}} k}{\eta L}(P_0 - P) + k_n^{\mathrm{eff}} Q. \tag{4}$$

where U is the relative displacement between the load point and the slider, $\dot{()}$ denotes time derivative, V_0 is the loading velocity, V

is slip rate, T is the vibration period, k_s is the shear stiffness, V_* is a normalizing slip rate, μ_* is a constant appropriate for steady-state at slip rate V_*, $\hat{a}$ and $\hat{b}$ are experimentally derived parameters relating friction to changes in slip rate and state, respectively, Θ is a state variable describing the sliding surface, Σ is the total stress, P is the pressure inside the slider (pore pressure), d_c is the characteristic slip distance, $\hat{\alpha}$ is a scaling factor ranging from 0 to μ[42,43], k_n^{eff} is the effective normal stiffness (related to the uniaxial bulk modulus or the reciprocal of the uniaxial specific storage per diffusion length in a continuum), k is the permeability, η is fluid dynamic viscosity, L is the pressure diffusion length, P_0 is the ambient pressure, and Q is the volumetric injection rate per unit area.

Choosing the following characteristic quantities: $u_c = d_c$, $v_c = V_*$, $\mu_c = \mu_*$, $p_c = P_0$, $\tau_c = \mu_*(\Sigma - P_0)$, $\theta_c = \mu_*$, and $t_c = d_c/V_*$, the equations describing the dynamic motion of the system, in dimensionless form, become (see Supplementary Note 2):

$$\dot{u} = v_0 - v, \tag{5}$$

$$\dot{v} = \frac{1}{\epsilon^2}\left[u - \frac{1}{\kappa}(1 + a\ln v + \theta)(\sigma - p)\right], \tag{6}$$

$$\dot{\theta} = -v(\theta + b\ln v) + \alpha\frac{\dot{p}}{(\sigma - p)}, \tag{7}$$

$$\dot{p} = c(p_0 - p) + rq, \tag{8}$$

where $\kappa = (k_s d_c)/\tau_c$, $a = \hat{a}/\mu_c$, $b = \hat{b}/\mu_c$, $\alpha = \hat{\alpha}/\mu_c$, $\epsilon = (T/2\pi)/t_c$, $c = t_c/(\eta L/k_n^{eff}/k)$, $r = t_c k_n^{eff}$, and $q = Q/p_c$. The parameter κ is the normalized shear stiffness, and a, b, α are normalized frictional parameters. The parameter ϵ is the normalized oscillation period or ratio of inertial to state-evolution timescales, which may range from 10^{-8} to 10^{-6} depending on rupture diameter and shear wave speed. The parameter c is the normalized diffusivity or ratio of the pore pressure to the state-evolution timescales, which may range from 10^{-4} to 10^{1} depending on reservoir permeability, uniaxial bulk modulus, and well-fault distance. The parameter rq is the normalized injection rate, which may range from 10^{-5} to 10^{-1} depending on injection rate and reservoir size.

Stability analysis. The stability of steady frictional sliding to small perturbations in velocity, which determines whether motion is by slow steady-sliding or violent stick-slip, depends on the evolution of the frictional resistance. Stick-slip occurs whenever a change of frictional resistance with sliding occurs at a rate greater than the loading system is capable of following[31]. At a constant pore pressure, linear stability analysis of the system about steady-state leads to the stability condition by Ruina[32]. Pore pressure, however, is not constant in time and its evolution depends on the injection rate and on the poroelastic and hydraulic parameters of the rupture. To quantify this, we carry out a linear stability analysis of the system about a quasi steady-state where sliding is steady but pore pressure is evolving as a result of fluid injection. We find that motion is by stick-slip when the dimensionless shear stiffness of the loading system is lower than a critical value ($\kappa < \kappa_{crit}$) given by

$$\kappa_{crit} = (b - a)(\sigma - p) + \frac{\alpha}{v_0}\dot{p}, \tag{9}$$

and is by steady-sliding otherwise ($\kappa > \kappa_{crit}$). Variables p and $\dot{p}$ are dimensionless pore pressure magnitude and pore pressure rate, respectively, at any point in time. Accordingly, frictional instability for the spring–poroslider system with an evolving pore pressure depends not only on the magnitude of pore pressure, but also on the rate of change of pore pressure (Supplementary Notes 3, 4, 5, and 6 for the analysis of QSSA, derivation of Eq. (9), and validation against nonlinear simulations).

As pore pressure evolves from initial to steady-state conditions in response to fluid injection, we find that the competing effects of p and $\dot{p}$ exhibit a transition in their dominance over frictional instability (Fig. 2a). The destabilizing effect of $\dot{p}$ dominates when pore pressure grows rapidly at early times, resulting in an increase in critical stiffness (dashed curve in Fig. 2a). It then decreases as pore pressure diffuses and approaches steady state, giving rise to the stabilizing effect of p, which explains the decrease in critical stiffness at late times (dotted curve in Fig. 2a). This result is generally consistent with a linear stability analysis of slow slip with mildly rate-strengthening friction in a poroelastic continuum[44], in which undrained slip-induced poroelastic pressure has a destabilizing effect and a sufficiently fast equilibration process has a stabilizing effect. In our analysis, the early-time destabilizing effect of $\dot{p}$ is likely attributed to a short-term effect

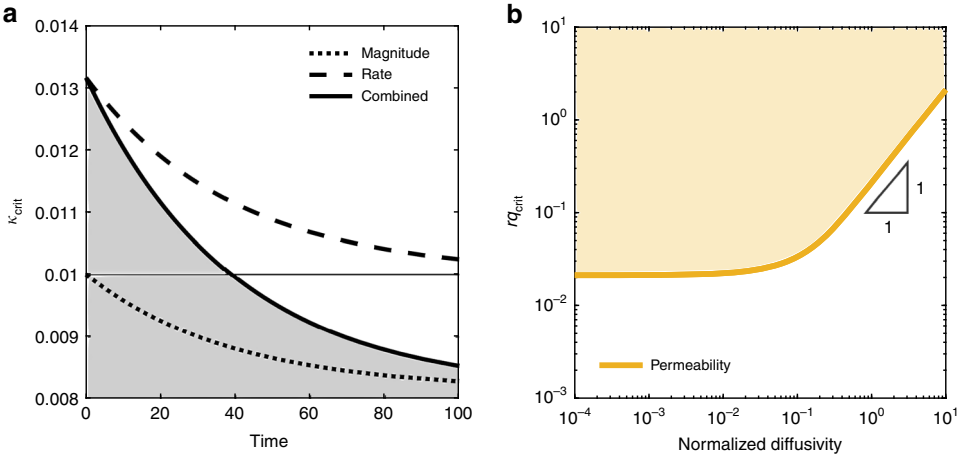

Fig. 2 Dimensionless critical stiffness and critical injection rate. a Critical stiffness—below which stick-slip instability is triggered ($\kappa < \kappa_{crit}$) and above which stick-slip instability is inhibited ($\kappa > \kappa_{crit}$)—in response to fluid injection at constant rate in velocity-weakening material ($c = 3 \times 10^{-2}$, $rq = 5 \times 10^{-3}$). The combined effect is illustrated by the solid curve, which shows a transition in the effect of fluid injection from de-stabilizing at early times to stabilizing at late times. The effect of the magnitude of pore pressure is illustrated by the dotted curve. The effect of the rate of change in pore pressure is illustrated by the dashed curve. **b** Critical injection rate—above which stick-slip instability is triggered—as a function of the normalized diffusivity of the system. The diffusivity is varied by varying permeability (beige curve in **b**).

on contact interlocking, where a decrease in effective normal stress results in fault opening and loss of asperity contacts[45]. The late-time stabilizing effect of p, in contrast, is likely attributed to a long-term effect on interface locking. A low effective normal stress tends to reduce the degree of interface locking, and thus limit the magnitude of stress drops[46–48].

This behavior is also qualitatively consistent with laboratory observations of sliding between saturated rocks at both transient and steady-state pore pressure conditions. The early-time destabilizing effect agrees with experimental studies showing that a gradual increase in pore pressure results in unstable slip during the transient-state, and that the degree of instability measured by the total slip, slip rate, and shear stress drop correlates with the rate of pore pressure increase[38,39]. The late-time stabilizing effect also agrees with another experimental study, showing that sliding between two rock surfaces is much more stable at high than at low steady-state pore pressure[40]. Sliding is observed to be by slow, steady-type motion at high pore pressure, and by stick-slip at low pore pressure. This behavior, however, is different from the observations of shearing granular fault gouge materials[49,50], where the frictional parameter $a-b$ is observed to decrease in magnitude with increasing steady-state pore pressure, an effect related to shear-induced dilatancy strengthening and pore compaction creep.

Application to the Denver earthquakes. Our findings, if they are applicable to natural faults, hold interesting and important implications for induced seismicity. The poroelastic spring–slider may be viewed as a simple model of a fault segment in contact with a reservoir, steady-sliding as an analog of aseismic creep, and stick-slip as a seismic wave-producing rupture cycle[33,37]. The spring stiffness scales inversely with the size of the fault segment[51]. Within this view, our findings may be generalized to indicate that a slowly creeping fault segment is destabilized and nucleates an earthquake if its size exceeds a critical value known as the nucleation length, which is inversely proportional to the critical stiffness in Eq. (9).

To bridge the gap between the analysis of the idealized poroelastic spring–slider model and the real world, we extend our instability criterion from dimensionless to dimensional form, and identify values of dimensionless parameters c and rq that correspond to a real-world setting. The 1960s Denver earthquakes is a good example of a real-world setting, where it is well-documented that injection of wastewater into the fractured Precambrian granite gneiss underneath the Rocky Mountain Arsenal triggered the earthquakes and where injection rate is directly related to the frequency of earthquakes[52,53]. We find that reasonable estimates of c and rq for this setting are in the order of 10^{-2} to 10^{-1} and 10^{-3} to 10^{-1}, respectively. We then assess the effect of fluid pressurization by evaluating its contribution to the critical stiffness in Eq. (9). We find that a reasonable estimate for the increase in critical stiffness at early times is ~300%, which indicates that the weakening effect from fluid pressurization is likely significant in this setting (see Supplementary Note 7 for more details on the application to the Denver earthquakes).

When earthquakes nucleate on a fault with velocity-weakening friction, in general, aseismic creep may begin in sections of favorable stress conditions. The aseismically creeping segment then slowly grows in size until it reaches the nucleation length, and then it breaks out rapidly into a seismic wave-producing rupture[54]. A significant increase in critical stiffness, or equivalently decrease in nucleation length, from fluid pressurization may further facilitate or exacerbate this breakout—potentially increasing the likelihood of triggering earthquakes.

Influence of reservoir properties on injection-induced seismicity. To study the influence of reservoir properties on the critical injection rate, above which earthquakes are induced, we model the occurrence of earthquakes as a function of dimensionless injection rate $rq = d_c k_n^{eff} Q/(p_c V_*)$ and normalized diffusivity $c = d_c k_n^{eff} k/(\eta L V_*)$ for velocity-weakening conditions, $b - a > 0$. We find that the dimensionless critical injection rate is directly proportional to the diffusivity c in the high-diffusivity limit, and independent of it in the low-diffusivity limit (Fig. 2b). These findings suggest that reservoir regions with low hydraulic diffusivity are more prone to induced seismicity than regions with high hydraulic diffusivity—a result that qualitatively agrees with the triggering-front concept[24] (see Supplementary Note 8 for more details on the phase diagram of injection-induced seismicity).

Influence of injection strategy on induced seismicity. The earthquake likelihood is strongly dependent on the duration of injection. For a fixed total injected volume, a shorter injection duration (or, equivalently, a higher injection rate) results in a higher likelihood of earthquake triggering (Supplementary Note 9).

To further understand how injection rate may be used to minimize or mitigate the seismic hazard, we simulate three different injection scenarios, and examine the stability of each. Figure 3 demonstrates how injecting the same volume of fluid can have very different seismic potential depending on the injection profile. We observe that injecting at constant rate in scenario (A) causes the critical stiffness to increase at early times, potentially triggering earthquakes, and decrease at late times, potentially resulting in the cessation of earthquakes. In addition, we observe a dramatic drop in critical stiffness upon stopping injection followed by recovery to the value prior to injection. Scenario (B) shows that a higher injection rate yields higher critical stiffness, implying an increased risk of seismicity for this higher injection rate. Scenario (C), where the injection rate ramps up in stages, seems to be most stable because the maximum critical stiffness is lower than its value in both (A) and (B). If the duration of each stage is not sufficiently long for pressure to stabilize at the fault, the ramp-up injection strategy does not counteract the destabilizing effect of the rate of pore pressure increase at each injection rate increment. In the Basel enhanced geothermal site, for example, the duration of injection stages was 1 day[55], while the time for pressure to stabilize at the fault is longer than 1 month—a conservative estimate based on the distance to the nearest fault segment to the injection well and the permeability of the fractured rock[25,55]. This suggests that a gradual increase in injection rate, where pore pressure is allowed to stabilize between injection stages, may be the safest injection strategy.

Summary and outlook. In summary, our model points to the underlying mechanism by which the rate of fluid pressurization, and hence the rate of effective normal stress unloading, may explain several injection-induced seismicity observations[1,11–14,16–18]. An abrupt or large increase in injection rate tends to intensify the early-time destabilizing effect of the rate of change in pore pressure on frictional sliding, whereas a gradual or small increase in injection rate tends to lessen it. Our findings, as a whole, suggest injection strategies to mitigate the seismic risk associated with a wide range of subsurface operations, from wastewater injection to geologic CO_2 sequestration. Of course, a complex interplay of different mechanisms such as heterogeneous fault stresses, stress changes from aseismic slip, spatial growth of pore pressure diffusion, and static and dynamic stress transfer often play a role in the occurrence and, in particular, the timing of an earthquake[4]. This emphasizes

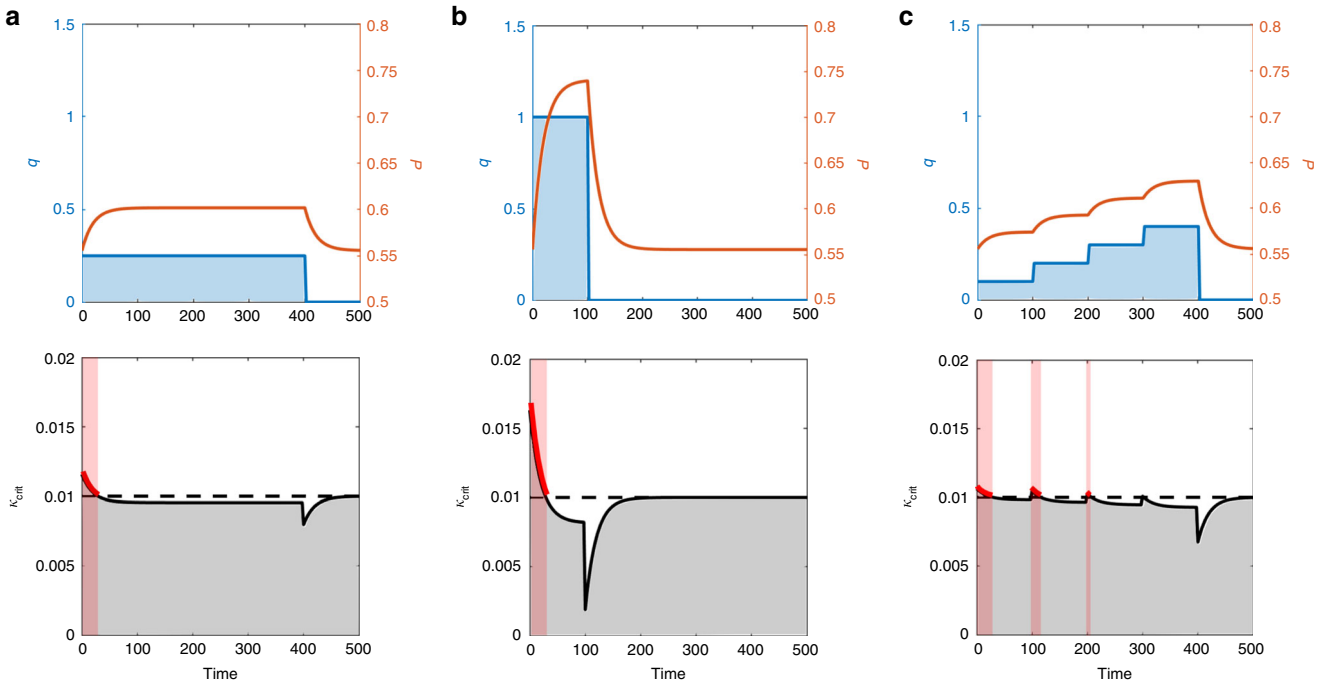

Fig. 3 Comparison of stability profiles for three different injection scenarios with the same total injected volume. a reference injection rate and period of injection ($c = 3 \times 10^{-2}$, $rq = 5 \times 10^{-3}$); **b** fourfold increase in injection rate, and corresponding fourfold decrease in the period of injection ($c = 3 \times 10^{-2}$, $rq = 2 \times 10^{-2}$); **c** linear ramp-up in injection rate over the same period of injection as the reference case ($c = 3 \times 10^{-2}$, $rq = 2 \times 10^{-3}$). The top figures show injection rates (blue) and pore pressures (orange). The bottom figures show the critical stiffness in response to the different injection scenarios (solid black) compared to the pre-injection critical stiffness value (dashed black). Higher peak in critical stiffness is indicative of higher likelihood for triggering earthquakes.

the need to continue to develop and test new models for the forecast and control of induced seismicity[10].

Methods

Methods described in the Supplementary Information. All methods and data are described in the Supplementary Information, including: (1) Derivation of the poroelastic spring–slider equations; (2) Governing equations in dimensionless form; (3) Linear stability analysis; (4) Nonlinear simulations; (5) Analytical vs. numerical estimates of critical stiffness; (6) Detailed discussion on the quasi-steady-state approximation; (7) Application to the Denver earthquakes; (8) Phase diagram of injection-induced seismicity; and (9) Earthquake likelihood vs. injection duration.

Data availability

All relevant data are available upon reasonable request from the authors.

Code availability

The simulation code is available upon reasonable request from the authors.

Received: 23 September 2019; Accepted: 20 May 2020;
Published online: 16 June 2020

References

1. Healy, J., Rubey, W., Griggs, D. & Raleigh, C. The Denver earthquakes. *Science* **161**, 1301–1310 (1968).
2. Keranen, K. M., Weingarten, M., Abers, G. A., Bekins, B. A. & Ge, S. Sharp increase in central Oklahoma seismicity since 2008 induced by massive wastewater injection. *Science* **345**, 448–451 (2014).
3. Yeck, W. L. et al. Oklahoma experiences largest earthquake during ongoing regional wastewater injection hazard mitigation efforts. *Geophys. Res. Lett.* **44**, 711–717 (2017).
4. Grigoli, F. et al. The November 2017 Mw 5.5 Pohang earthquake: a possible case of induced seismicity in South Korea. *Science* **360**, 1003–1006 (2018).
5. Raleigh, C., Healy, J. & Bredehoeft, J. An experiment in earthquake control at Rangely, Colorado. *Science* **191**, 1230–1237 (1976).
6. Hubbert, K. M. & Rubey, W. W. Role of fluid pressure in mechanics of overthrust faulting: I. mechanics of fluid-filled porous solids and its application to overthrust faulting. *Geol. Soc. Am. Bull.* **70**, 115–166 (1959).
7. Davis, S. D. & Pennington, W. D. Induced seismic deformation in the Cogdell oil field of West Texas. *Bull. Seismol. Soc. Am.* **79**, 1477–1495 (1989).
8. Hofmann, H. et al. First field application of cyclic soft stimulation at the Pohang Enhanced Geothermal System site in Korea. *Geophys. J. Int.* **217**, 926–949 (2019).
9. McGarr, A. Maximum magnitude earthquakes induced by fluid injection. *J. Geophys. Res. Solid Earth* **119**, 1008–1019 (2014).
10. Lee, K.-K. et al. Managing injection-induced seismic risks. *Science* **364**, 730–732 (2019).
11. Frohlich, C. Two-year survey comparing earthquake activity and injection-well locations in the Barnett Shale, Texas. *Proc. Natl Acad. Sci. USA* **109**, 13934–13938 (2012).
12. Weingarten, M., Ge, S., Godt, J. W., Bekins, B. A. & Rubinstein, J. L. High-rate injection is associated with the increase in US mid-continent seismicity. *Science* **348**, 1336–1340 (2015).
13. Improta, L., Valoroso, L., Piccinini, D. & Chiarabba, C. A detailed analysis of wastewater-induced seismicity in the Val d'Agri oil field (Italy). *Geophys. Res. Lett.* **42**, 2682–2690 (2015).
14. Langenbruch, C. & Zoback, M. D. How will induced seismicity in Oklahoma respond to decreased saltwater injection rates? *Sci. Adv.* **2**, e1601542 (2016).
15. Barbour, A. J., Norbeck, J. H. & Rubinstein, J. L. The effects of varying injection rates in Osage County, Oklahoma, on the 2016 M_w 5.8 Pawnee earthquake. *Seismol. Res. Lett.* **88**, 1040–1053 (2017).
16. Cuenot, N., Dorbath, C. & Dorbath, L. Analysis of the microseismicity induced by fluid injections at the EGS site of Soultz-sous-Forêts (Alsace, France): implications for the characterization of the geothermal reservoir properties. *Pure Appl. Geophys.* **165**, 797–828 (2008).
17. Kim, W.-Y. Induced seismicity associated with fluid injection into a deep well in Youngstown, Ohio. *J. Geophys. Res. Solid Earth* **118**, 3506–3518 (2013).
18. Tang, L., Lu, Z., Zhang, M., Sun, L. & Wen, L. Seismicity induced by simultaneous abrupt changes of injection rate and well pressure in Hutubi gas field. *J. Geophys. Res. Solid Earth* **123**, 5929–5944 (2018).
19. Langenbruch, C., Weingarten, M. & Zoback, M. D. Physics-based forecasting of man-made earthquake hazards in Oklahoma and Kansas. *Nat. Commun.* **9**, 3946 (2018).

20. Norbeck, J. & Rubinstein, J. L. Hydromechanical earthquake nucleation model forecasts onset, peak, and falling rates of induced seismicity in Oklahoma and Kansas. *Geophys. Res. Lett.* **45**, 2963–2975 (2018).
21. Zhai, G., Shirzaei, M., Manga, M. & Chen, X. Pore-pressure diffusion, enhanced by poroelastic stresses, controls induced seismicity in Oklahoma. *Proc. Natl Acad. Sci. USA* **116**, 16228–16233 (2019).
22. Torberntsson, K., Stiernström, V., Mattsson, K. & Dunham, E. M. A finite difference method for earthquake sequences in poroelastic solids. *Comput. Geosci.* **22**, 1351–1370 (2018).
23. Pampillón, P., Santillán, D., Mosquera, J. C. & Cueto-Felgueroso, L. Dynamic and quasi-dynamic modeling of injection-induced earthquakes in poroelastic media. *J. Geophys. Res. Solid Earth* **123**, 5730–5759 (2018).
24. Shapiro, S. & Dinske, C. Scaling of seismicity induced by nonlinear fluid-rock interaction. *J. Geophys. Res. Solid Earth* https://doi.org/10.1029/2008JB006145 (2009).
25. Majer, E. L. et al. Induced seismicity associated with enhanced geothermal systems. *Geothermics* **36**, 185–222 (2007).
26. Guglielmi, Y., Cappa, F., Avouac, J.-P., Henry, P. & Elsworth, D. Seismicity triggered by fluid injection–induced aseismic slip. *Science* **348**, 1224–1226 (2015).
27. Cornet, F., Helm, J., Poitrenaud, H. & Etchecopar, A. Seismic and aseismic slips induced by large-scale fluid injections. *Pure Appl. Geophys.* **150**, 563–583 (1997).
28. Bourouis, S. & Bernard, P. Evidence for coupled seismic and aseismic fault slip during water injection in the geothermal site of Soultz (France), and implications for seismogenic transients. *Geophys. J. Int.* **169**, 723–732 (2007).
29. Zoback, M. D. et al. The importance of slow slip on faults during hydraulic fracturing stimulation of shale gas reservoirs. *In SPE Americas Unconventional Resources Conference* (Society of Petroleum Engineers, 2012).
30. Wei, S. et al. The 2012 Brawley swarm triggered by injection-induced aseismic slip. *Earth Planet. Sci. Lett.* **422**, 115–125 (2015).
31. Byerlee, J. The mechanics of stick-slip. *Tectonophysics* **9**, 475–486 (1970).
32. Ruina, A. Slip instability and state variable friction laws. *J. Geophys. Res. Solid Earth* **88**, 10359–10370 (1983).
33. Rice, J. R. & Tse, S. T. Dynamic motion of a single degree of freedom system following a rate and state dependent friction law. *J. Geophys. Res. Solid Earth* **91**, 521–530 (1986).
34. Segall, P. & Rice, J. R. Dilatancy, compaction, and slip instability of a fluid-infiltrated fault. *J. Geophys. Res. Solid Earth* **100**, 22155–22171 (1995).
35. Iverson, R. M. Regulation of landslide motion by dilatancy and pore pressure feedback. *J. Geophys. Res. Earth Surf.* **110**, F02015 (2005).
36. Dieterich, J. H. Modeling of rock friction: 1. Experimental results and constitutive equations. *J. Geophys. Res. Solid Earth* **84**, 2161–2168 (1979).
37. Brace, W. & Byerlee, J. Stick-slip as a mechanism for earthquakes. *Science* **153**, 990–992 (1966).
38. Wang, L. et al. Laboratory study on fluid-induced fault slip behavior: The role of fluid pressurization rate. *Geophys. Res. Lett.* **47**, e2019GL086627 (2020).
39. French, M. E., Zhu, W. & Banker, J. Fault slip controlled by stress path and fluid pressurization rate. *Geophys. Res. Lett.* **43**, 4330–4339 (2016).
40. Byerlee, J. & Brace, W. Fault stability and pore pressure. *Bull. Seismol. Soc. Am.* **62**, 657–660 (1972).
41. Marone, C. Laboratory-derived friction laws and their application to seismic faulting. *Annu. Rev. Earth Planet. Sci.* **26**, 643–696 (1998).
42. Linker, M. & Dieterich, J. H. Effects of variable normal stress on rock friction: observations and constitutive equations. *J. Geophys. Res. Solid Earth* **97**, 4923–4940 (1992).
43. Kilgore, B., Lozos, J., Beeler, N. & Oglesby, D. Laboratory observations of fault strength in response to changes in normal stress. *J. Appl. Mech.* **79**, 031007 (2012).
44. Heimisson, E. R., Dunham, E. M. & Almquist, M. Poroelastic effects destabilize mildly rate-strengthening friction to generate stable slow slip pulses. *J. Mech. Phys. Solids* **130**, 262–279 (2019).
45. Wang, W. & Scholz, C. Micromechanics of the velocity and normal stress dependence of rock friction. *Pure Appl. Geophys.* **143**, 303–315 (1994).
46. Moreno, M., Rosenau, M. & Oncken, O. 2010 Maule earthquake slip correlates with pre-seismic locking of Andean subduction zone. *Nature* **467**, 198–202 (2010).
47. Kitajima, H. & Saffer, D. M. Elevated pore pressure and anomalously low stress in regions of low frequency earthquakes along the Nankai Trough subduction megathrust. *Geophys. Res. Lett.* **39**, L23301 (2012).
48. Segall, P., Rubin, A. M., Bradley, A. M. & Rice, J. R. Dilatant strengthening as a mechanism for slow slip events. *J. Geophys. Res. Solid Earth* https://doi.org/10.1029/2010JB007449 (2010).
49. Sawai, M., Niemeijer, A. R., Plümper, O., Hirose, T. & Spiers, C. J. Nucleation of frictional instability caused by fluid pressurization in subducted blueschist. *Geophys. Res. Lett.* **43**, 2543–2551 (2016).
50. Scuderi, M. M. & Collettini, C. The role of fluid pressure in induced vs. triggered seismicity: Insights from rock deformation experiments on carbonates. *Sci. Rep.* **6**, 24852 (2016).
51. Scholz, C. H. Earthquakes and friction laws. *Nature* **391**, 37 (1998).
52. Evans, D. M. The Denver area earthquakes and the Rocky Mountain Arsenal disposal well. *Mt. Geologist* **3**, 23–36 (1966).
53. Healy, J., Rubey, W., Griggs, D. & Raleigh, C. The Denver earthquakes. *Science* **161**, 1301–1310 (1968).
54. Perfettini, H., Schmittbuhl, J., Rice, J. R. & Cocco, M. Frictional response induced by time-dependent fluctuations of the normal loading. *J. Geophys. Res. Solid Earth* **106**, 13455–13472 (2001).
55. Häring, M. O., Schanz, U., Ladner, F. & Dyer, B. C. Characterisation of the Basel 1 enhanced geothermal system. *Geothermics* **37**, 469–495 (2008).

Acknowledgements

M.A. was supported by a graduate fellowship from Saudi Aramco. R.J. acknowledges funding from ExxonMobil through its membership in the MIT Energy Initiative.

Author contributions

R.J. designed research; M.A. performed research; M.A. and R.J. analyzed results; and M.A. and R.J. wrote the paper.

Competing interests

The authors declare no competing interests.

Additional information

Supplementary information is available for this paper at https://doi.org/10.1038/s41467-020-16860-y.

Correspondence and requests for materials should be addressed to R.J.

Peer review information *Nature Communications* thanks Matthew Weingarten and the other, anonymous, reviewer(s) for their contribution to the peer review of this work. Peer review reports are available.

Reprints and permission information is available at http://www.nature.com/reprints

Publisher's note Springer Nature remains neutral with regard to jurisdictional claims in published maps and institutional affiliations.

Supplementary Information for

Understanding rate effects in injection-induced earthquakes

Maryam Alghannam[1] and Ruben Juanes[1,2*]

[1]Department of Civil and Environmental Engineering,
Massachusetts Institute of Technology, Cambridge, MA 02139, USA
[2]Department of Earth, Atmospheric and Planetary Sciences,
Massachusetts Institute of Technology, Cambridge, MA 02139, USA

[*]To whom correspondence should be addressed; E-mail: juanes@mit.edu.

Supplementary Note 1

Derivation of the poroelastic spring–slider equations

Frictional evolution

Frictional evolution is modeled by the rate-and-state constitutive laws, which are capable of reproducing a wide range of observed seismic and aseismic fault behaviors ranging from preseismic slip and earthquake nucleation to coseismic rupture and earthquake after slip [1, 2, 3, 4]. These laws propose that frictional shear stress τ can be described as

$$\tau = \mu(V, \Theta)\Sigma', \tag{1}$$

where Σ' is the effective normal stress (the difference between total normal stress and pore pressure), μ is the coefficient of friction, V is the slider's velocity or slip rate, and Θ is a state variable with the physical interpretation of the fractional contact area that is associated with time dependent creep [5]. It is also related to the age of asperity contacts.

We adopt Ruina's [3] slip law for the coefficient of friction because it fits experimental data at variable normal stress better than Dieterich's [1] aging law [6],

$$\mu(V, \Theta) = \mu_* + \hat{a} \ln \frac{V}{V_*} + \Theta, \tag{2}$$

where $\hat{a}$ is an experimentally derived parameter, V_* is a normalizing velocity, and μ_* is a constant appropriate for steady-state at velocity V_*. Laboratory experiments on dry rocks show that a step change in normal stress results in a sudden change in the coefficient of friction followed by a displacement-dependent decay back toward the initial steady-state value [7, 5, 8, 9]. Linker and Dieterich [5] interpret this as due to a normal stress effect on the state variable and propose to model the magnitude of the sudden change as $\hat{\alpha}\dot{\Sigma}/\Sigma$. Although the model is based on step test experiments, it captures, at least qualitatively, the pressurization-weakening effect on the coefficient of friction observed from ramping

experiments by Olsson [7]. He performed laboratory tests in which the normal stress was increased at constant rate while the load point speed was held constant. He found that shear stress is a function of the normal stress rate. When the normal stress rate was increased by 10 during steady sliding, the rate of increase of shear stress with normal stress (coefficient of friction) decreased by a factor of two—a significant effect.

Here, we combine the proposed state evolution model with the effective stress principle to get

$$\dot{\Theta} = -\frac{V}{d_c}(\Theta + \hat{b}\ln\frac{V}{V_*}) - \hat{\alpha}\frac{\dot{\Sigma}'}{\Sigma'}, \tag{3}$$

where d_c is the characteristic sliding distance required to replace the old contact population with a new one, $\hat{b}$ is a constitutive parameter, and $\hat{\alpha}$ is a scaling factor. Theoretical and laboratory studies for a sudden change in normal stress show that $\hat{\alpha}$ ranges from 0 to μ [5, 10, 11], but more studies are needed to determine the value of $\hat{\alpha}$ for a gradual change in normal stress. From momentum balance of forces acting on the slider, the equations of motion of the system evolution at variable effective normal stress become

$$\dot{U} = V_0 - V, \tag{4}$$

$$\dot{V} = \frac{1}{(T/2\pi)^2}\left[U - \frac{1}{k_s}\mu(V,\Theta)\Sigma'\right], \tag{5}$$

where $T = 2\pi\sqrt{m/k_s}$ is the vibration period of the analogous freely slipping system [12].

Poroelastic coupling

To obtain a physical evolution of effective stress on the frictional surface, we couple it with a poroelastic model of pore pressure and rock deformation. Starting with the principle of mass conservation, we specify the change of mass from fluid diffusion to be Δm_{diff}, mass accumulation due to rock expansion or fluid compressibility $\frac{\partial}{\partial t}(\rho V_f)\Delta t$, and injection source term to be $\tilde{Q}\Delta t$. We assume that both the fluid and rock matrix are

compressible [13], and so mass balance leads to

$$\Delta m_{\text{diff}} = \frac{\partial(\rho V_{\text{f}})}{\partial t}\Delta t - \tilde{Q}\Delta t, \tag{6}$$

where the change in fluid mass due to pressure diffusion can be written using Darcy's law as

$$\Delta m_{\text{diff}} = -\frac{\rho k A(P - P_0)}{\eta L}\Delta t, \tag{7}$$

where η is fluid dynamic viscosity, k is permeability, and L is the pressure diffusion length. The mass accumulation term can be expressed as

$$\frac{\partial}{\partial t}\rho V_{\text{f}}\Delta t = \frac{\partial}{\partial t}\rho(P)HA\Delta t = \frac{\partial}{\partial t}(\rho_0(1 + c_{\text{f}}(P - P_0))(H_0 + W)A\Delta t, \tag{8}$$

where H is the current height of the slider, ρ_0 is the initial fluid density, c_{f} is fluid compressiblity, H_0 is the initial height of the slider, and W is the position of the piston. When fluid is injected into a rock that is free to deform in the direction orthogonal to sliding, the addition of mass induces an increase of volume equivalent to

$$V_{\text{f}} - V_{\text{f},0} = AW, \tag{9}$$

where $V_{\text{f},0}$ is the initial fluid volume. We then derive an expression for rock deformation W from force balance, while using the convention of compression positive,

$$W = \frac{A}{k_{\text{n}}}(\Sigma_0' - \Sigma + P), \tag{10}$$

where k_{n} is the normal spring stiffness and Σ_0' is the initial effective stress. We further approximate the mass accumulation term to

$$\rho\frac{\partial}{\partial t}[AH]\Delta t + AH\frac{\partial P}{\partial t}\Delta t = \rho\frac{A}{k_{\text{n}}}\frac{\partial P}{\partial t}\Delta t + H\frac{\rho_0}{\rho}c_{\text{f}}\frac{\partial P}{\partial t}\Delta t \approx \rho\frac{A}{k_{\text{n}}}\frac{\partial P}{\partial t}\Delta t + H_0 c_{\text{f}}\frac{\partial P}{\partial t}\Delta t. \tag{11}$$

Note that we consider that the total stress Σ is analogous to overburden stress in the earth, and is therefore constant in time. By substituting Eqs. (7)-(10) into Eq. (6), we

find that pore pressure satisfies a diffusion equation that leads to transient behavior at early times and steady-state behavior at late times

$$\dot{P} = \frac{k_{\mathrm{n}}^{\mathrm{eff}} k}{\eta L A}(P_0 - P) + \frac{k_{\mathrm{n}}^{\mathrm{eff}}}{A} Q, \tag{12}$$

where η is fluid dynamic viscosity ($\eta = \nu\rho$), Q is the volumetric injection rate per unit area ($Q = \tilde{Q}/\rho A$), and $k_{\mathrm{n}}^{\mathrm{eff}} = (1/k_{\mathrm{n}} + c_{\mathrm{f}} H_0/A)^{-1}$ is an effective stiffness somewhat equivalent to the uniaxial bulk modulus or the reciprocal of the uniaxial specific storage per diffusion length in a continuum [13]. Since the slider has a unit base area ($A = 1$), the evolution of the pore pressure as a result of fluid injection follows

$$\dot{P} = \frac{k_{\mathrm{n}}^{\mathrm{eff}} k}{\eta L}(P_0 - P) + k_{\mathrm{n}}^{\mathrm{eff}} Q. \tag{13}$$

Supplementary Note 2

Governing equations in dimensionless form

The equations describing the dynamic motion of the spring-poroslider system (Figure. 1B) with an evolving pore pressure, in dimensional form, are

$$\dot{U} = V_0 - V, \tag{14}$$

$$\dot{V} = \frac{1}{(T/2\pi)^2}\left[U - \frac{1}{k_\mathrm{s}}(\mu_* + \hat{a}\ln\frac{V}{V_*} + \Theta)(\Sigma - P)\right], \tag{15}$$

$$\dot{\Theta} = -\frac{V}{d_\mathrm{c}}(\Theta + \hat{b}\ln\frac{V}{V_*}) + \hat{\alpha}\frac{\dot{P}}{(\Sigma - P)}, \tag{16}$$

$$\dot{P} = \frac{k_\mathrm{n}^\mathrm{eff} k}{\eta L}(P_0 - P) + k_\mathrm{n}^\mathrm{eff} Q. \tag{17}$$

Choosing the following characteristic quantities: $u_\mathrm{c} = d_\mathrm{c}$, $v_\mathrm{c} = V_*$, $\mu_\mathrm{c} = \mu_*$, $p_\mathrm{c} = P_0$, $\tau_\mathrm{c} = \mu_*(\Sigma - P_0)$, $\theta_\mathrm{c} = \mu_*$, and $t_\mathrm{c} = d_\mathrm{c}/V_*$, the equations describing the dynamic motion of the system, in dimensionless form, become

$$\dot{u} = v_0 - v, \tag{18}$$

$$\dot{v} = \frac{1}{\epsilon^2}\left[u - \frac{1}{\kappa}(1 + a\ln v + \theta)(\sigma - p)\right], \tag{19}$$

$$\dot{\theta} = -v(\theta + b\ln v) + \alpha\frac{\dot{p}}{(\sigma - p)}, \tag{20}$$

$$\dot{p} = c(p_0 - p) + rq, \tag{21}$$

where $\kappa = (k_\mathrm{s} d_\mathrm{c})/\tau_\mathrm{c}$, $a = \hat{a}/\mu_\mathrm{c}$, $b = \hat{b}/\mu_\mathrm{c}$, $\alpha = \hat{\alpha}/\mu_\mathrm{c}$, $\epsilon = (T/2\pi)/t_\mathrm{c}$, $c = t_\mathrm{c}/(\eta L/k_\mathrm{n}^\mathrm{eff}/k)$, $r = t_\mathrm{c} k_\mathrm{n}^\mathrm{eff}$, and $q = Q/p_\mathrm{c}$. The parameter κ is the normalized shear stiffness, and a, b, α are normalized frictional parameters. The parameter ϵ is the normalized oscillation period or ratio of inertial to state-evolution timescales, which may range from 10^{-8} to 10^{-6} depending on rupture diameter and shear wave speed. The parameter c is the normalized diffusivity or ratio of the pore-pressure to the state-evolution timescales, which may range

from 10^{-4} to 10^{1} depending on reservoir permeability, bulk modulus (storativity), and well-fault distance. The parameter rq is the normalized injection rate, which may range from 10^{-5} to 10^{-1} depending on injection rate and reservoir size.

Supplementary Note 3

Linear stability analysis

The stability of steady frictional sliding to small perturbations in velocity depends on the state of pore pressure. For a constant pore pressure, linear stability analysis leads to the steady-state stability condition by Ruina (1983) [3], which shows that the slider is stable when the dimensionless spring stiffness of the loading system exceeds a critical value given by

$$\kappa_{\mathrm{crit}} = (b - a)(\sigma - p), \tag{22}$$

and it is unstable otherwise. Pore pressure, however, is not constant in time, and its evolution depends on the injection rate and on the poroelastic and hydraulic parameters of the rupture (Eq. (21)). A common approach to stability analysis with time-varying state variables is the use of the quasi-steady-state approximation [14, 15, 16, 17]. Using this approach, we freeze time in the pore pressure solution and then perform a linear stability analysis of the spring–poroslider system at a fixed pore pressure.

The equations describing the quasi-static motion of the spring–poroslider system evolving at variable pore pressure p, in dimensionless form, are

$$\dot{u} = v_0 - v, \tag{23}$$

$$0 = (\sigma - p)\mu(v, \theta) - \kappa u, \tag{24}$$

$$\dot{\theta} = -v(b \ln v + \theta) + \alpha \frac{\dot{p}}{(\sigma - p)}. \tag{25}$$

The quasi-steady-state values of the variables are $v_{\mathrm{qss}} = v_0$ and $\theta_{\mathrm{qss}} = \alpha\dot{p}/(\sigma - p)/v_0 - b \ln v_0$. Linearizing Eqs. (23)–(25) about the quasi-steady-state, and then taking the time

derivative of Eq. (24), yields

$$\Delta\dot{v} = \frac{v_0}{a}\left[b + \frac{\alpha}{v_0}\frac{\dot{p}}{(\sigma - p)} - \frac{\kappa}{(\sigma - p)}\right]\Delta v + \frac{v_0^2}{a}\Delta\theta, \tag{26}$$

$$\Delta\dot{\theta} = -\left[b + \frac{\alpha}{v_0}\frac{\dot{p}}{(\sigma - p)}\right]\Delta v - v_0\Delta\theta. \tag{27}$$

Equations (26)–(27) represent a 2×2 system of autonomous linear ODEs with solutions of the form $\Delta v = Ve^{\lambda t}$, $\Delta\theta = \Theta e^{\lambda t}$, where λ is the growth rate and t is time. Substituting these forms into the linearized equations (26)–(27) yields the characteristic equation

$$a(\sigma - p)\lambda^2 + (-\alpha\dot{p} + \kappa v_0 - (b - a)(\sigma - p)v_0)\lambda + \kappa v_0^2 = 0. \tag{28}$$

If the real part of the roots λ_i are negative for all i, perturbations from the quasi-steady-state are damped and the system is stable. If the real part of the roots λ_i are positive for some i, then perturbations grow exponentially and the system is unstable. At $\Re(\lambda_\mathrm{i}) = 0$, we find that the dimensionless critical stiffness is

$$\kappa_\mathrm{crit} = (b - a)(\sigma - p) + \frac{\alpha}{v_0}\dot{p}. \tag{29}$$

If we express the instability condition (Eq. (29)) in terms of a critical dimensionless injection rate, above which an earthquake is induced, we obtain

$$rq_\mathrm{crit} = \frac{\kappa - (b - a)(\sigma - p_0)}{\frac{\alpha}{v_0}e^{-ct} - \frac{b-a}{c}(1 - e^{-ct})}. \tag{30}$$

Supplementary Note 4

Nonlinear simulations

To validate our analytical instability criterion (Eq. (29)), we simulate the fully dynamic equations of motion of the spring–poroslider system (Eqs. (18)-(21)) with the following initial conditions

$$u(t=0) = v_0(\sigma - p_0)(1 + (a-b)\ln v_0)/\kappa, \tag{31}$$

$$v(t=0) = v_0, \tag{32}$$

$$\theta(t=0) = 0, \tag{33}$$

$$p(t=0) = p_0. \tag{34}$$

These coupled nonlinear ordinary differential equations are solved in MATLAB using the `ode15s` solver for stiff systems. Representative results of motion without fluid injection and motion while fluid is being injected into the poroslider at a constant rate are shown in Supplementary Figures 1 and 2, respectively.

The simulation without fluid injection is performed using parameter values $a = 0.01$, $b = 0.02$, $\alpha = 1$, $\epsilon = 10^{-6}$, $c = 3\times10^{-2}$, and $\kappa = 0.011$. The simulation with fluid injection is performed using the same parameter values along with $rq = 5 \times 10^{-3}$. The poroslider is initially sliding steadily at a fixed loading velocity $v_0 = 1$ and a zero fluid injection rate $q = 0$. It is then made unstable by suddenly increasing the loading velocity to a new fixed value $v_0 = 1.5$ and injecting fluid at a constant rate $q = 10^{-9}$. This triggers two stick-slip events, consisting of a slow build-up followed by a sudden discharge of accumulated stress. The buildup occurs at a nearly stationary state $v \approx 0.1$ over a time period of 15, whereas the discharge is significantly faster reaching a peak velocity $v \approx 10^7$, and has a duration of 0.5 (Supplementary Figure 2A). Following the two stick-slip events, the poroslider evolves toward steady sliding at a relatively low and constant velocity $v \approx 1.5$.

The normalized stress variations with velocity, slip, and time are shown in Supplementary Figure 2B. Initially, the sudden change in load point velocity and effective normal stress creates an excess of spring force over the frictional resistance, which in turn accelerates the poroslider. The stress drops to a steady state value corresponding to slip velocity. The poroslider continues to slip at a high rate until further shortening of the spring becomes too difficult. It then decelerates to reach a nearly stationary state. During this stage, the stress builds up to a peak value corresponding to stick velocity, and the stick-slip cycle repeats. Note that the cycle is not repeated exactly, the stress buildup after a slip event is dependent on the current effective normal stress. Eventually, the decrease in effective normal stress terminates the stick-slip cycle and initiates an indefinite period of steady-sliding. The stress exhibits decaying oscillations that decrease in amplitude with time.

Supplementary Note 5

Analytical vs numerical estimates of critical stiffness

As a whole, Supplementary Figure 2 shows that the analytical critical stiffness (Eq. (29)) is in good qualitative agreement with the numerical simulation results. To validate our instability criterion quantitatively, we compare our instability criterion against estimates obtained empirically from the fully dynamic nonlinear simulations (Supplementary Figure 3). The analytical estimate (blue) works well when the growth rate of perturbations is large compared to the growth rate of the pore pressure. Initially, when pore pressure grows rapidly, estimates differ slightly, but they become indistinguishable at late times, when pore pressure changes relatively slowly. We suspect that the small difference in estimates at early times is due to, at least partially, the use of the QSSA in our analysis, which we discuss in detail in Supplementary Note 6.

Supplementary Note 6

Quasi-steady-state approximation

The quasi-steady-state approximation, in general, is an approach to simplify dynamic systems of ordinary differential equations with an initial fast transient, after which some of the dependent variables can be assumed to be in steady-state with regard to the other slowly evolving dependent variables [16]. In particular, the QSSA is a good approach to use in our analysis because it allows us to study the stability of steady frictional sliding to small perturbations in velocity while pore pressure is evolving. The sliding velocity and the velocity-dependent part of the state variable are in steady state with respect to the pore pressure. Here, we analyze the QSSA in the context of singular perturbation theory following the analysis by Segel and Slemrod (1989) [16], identify the small parameter(s) necessary for the validity of the QSSA, and quantify the error associated with it.

Reduced dimensional equations

As shown in Supplementary Note 1, the dynamics of our poroelastic spring-slider model is governed by a system of four coupled nonlinear ODEs. Under quasi-static loading, velocity is the fastest evolving variable of the system and it responds instantaneously (negligible inertia) to small perturbations. Thus we can focus our analysis on a reduced system of ODEs at steady-state velocity $V = V_0$,

$$\dot{\Theta} = -\frac{V_0}{d_c}(\Theta + \hat{b}\ln\frac{V_0}{V_*}) + \hat{\alpha}\frac{\dot{P}}{\Sigma - P}, \tag{35}$$

$$\dot{P} = \frac{k_n^{\text{eff}} k}{\eta L}(P_0 - P) + k_n^{\text{eff}} Q, \tag{36}$$

with initial conditions

$$\Theta(0) = 0, \tag{37}$$

$$P(0) = P_0. \tag{38}$$

Timescales

As a first step in the analysis, we estimate the fast timescale t_Θ of the pre-steady-state period and the slow timescale t_P for the evolution of pore pressure. To estimate t_Θ we make the approximation $P \approx P_0$ in Eq. (35). The solution for the state variable becomes

$$\Theta(t) = \bar{\Theta}(e^{-\frac{V_0}{d_\mathrm{c}}t} - 1), \tag{39}$$

where $\bar{\Theta} = \hat{b} \ln V_0/V_* - \hat{\alpha}(d_\mathrm{c}/V_0)(\dot{P}_0/(\Sigma - P_0))$. Subsequently, we take

$$t_\Theta = \frac{d_\mathrm{c}}{V_0}. \tag{40}$$

Since the pore pressure evolution is independent of the evolution of the state variable Θ, we estimate t_P by solving Eq. (36) with the initial condition $P(0) = P_0$ to obtain

$$P(t) = P_0 + \frac{\eta L}{k} Q(1 - e^{-\frac{k_\mathrm{n}^\mathrm{eff} k}{\eta L}t}). \tag{41}$$

Similarly, we take

$$t_\mathrm{P} = \frac{\eta L}{k_\mathrm{n}^\mathrm{eff} k}. \tag{42}$$

Scaled dimensionless equations

During the pre-steady-state, it is reasonable to scale time by t_Θ, where the dimensionless time τ is given by

$$\tau = \frac{t}{t_\Theta}. \tag{43}$$

Thus, the scaled dimensionless governing equations become

$$\frac{\partial \theta}{\partial \tau} = -v_0(\theta + b \ln v_0) + \frac{\alpha}{\sigma - p}\frac{\partial p}{\partial \tau}, \tag{44}$$

$$\frac{\partial p}{\partial \tau} = \frac{t_\Theta}{t_\mathrm{P}}(p_0 - p) + t_\Theta q, \tag{45}$$

with initial conditions

$$\theta(0) = 0, \tag{46}$$

$$p(0) = p_0, \tag{47}$$

where we have defined $b = \hat{b}/\mu_0$, $\alpha = \hat{\alpha}/\mu_0$, and $q = Q/p_0$. After the pre-steady state, the QSSA is assumed to be valid and t_P becomes a reasonable timescale. We introduce a new dimensionless scaled time $\tilde{t}$ by

$$\tilde{t} = \frac{t}{t_\mathrm{P}}, \tag{48}$$

with which the scaled dimensionless governing equations become

$$\frac{t_\Theta}{t_\mathrm{P}}\frac{\partial \theta}{\partial \tilde{t}} = -v_0(\theta + b \ln v_0) + \frac{t_\Theta}{t_\mathrm{P}}\frac{\alpha}{\sigma - p}\frac{\partial p}{\partial \tilde{t}}, \tag{49}$$

$$\frac{\partial p}{\partial \tilde{t}} = (p_0 - p) + t_\mathrm{P} q. \tag{50}$$

Singular perturbation

Approximate solutions can now be obtained by methods of singular perturbation theory [18], for $0 < t_\Theta/t_\mathrm{P} \ll 1$. A solution of Eqs. (44)-(45) is obtained of the form

$$\theta(\tau) = \theta^{(0)}(\tau) + \frac{t_\Theta}{t_\mathrm{P}}\,\theta^{(1)}(\tau) + ..., \tag{51}$$

$$p(\tau) = p^{(0)}(\tau) + \frac{t_\Theta}{t_\mathrm{P}}\,p^{(1)}(\tau) + ..., \tag{52}$$

where

$$\theta^{(0)}(\tau) = \bar{\theta}(e^{-\tau} - 1), \tag{53}$$

$$p^{(0)}(\tau) = p_0. \tag{54}$$

Similarly, the solution of Eqs. (49)-(50) obtained of the form

$$\theta(\tilde{t}) = \theta_0(\tilde{t}) + \frac{t_\Theta}{t_\mathrm{P}}\,\theta_1(\tilde{t}) + \ldots\,, \tag{55}$$

$$p(\tilde{t}) = p_0(\tilde{t}) + \frac{t_\Theta}{t_\mathrm{P}} p_1(\tilde{t}) + \ldots\,, \tag{56}$$

where

$$\theta_0 = -b\ln v_0 + \frac{\alpha}{v_0}\frac{t_\Theta q}{\sigma - p_0}, \tag{57}$$

$$\frac{\partial p_0}{\partial \tilde{t}} = t_\mathrm{P} q. \tag{58}$$

Note that Eqs. (57)-(58) are associated with initial conditions Eqs. (37)-(38), and represent the initial state about which we linearized the spring-poroslider system (section 3). The results of this analysis remain valid for general initial conditions $\Theta(0) = \Theta_\mathrm{i}$ and $P(0) = P_\mathrm{i}$ [16], where Θ_i ranges from 0 to Θ_ss and P_i ranges from P_0 to P_ss. Linearizing the spring-poroslider system about the true steady-state, where

$$\theta_0 = -b\ln v_0, \tag{59}$$

$$\frac{\partial p_0}{\partial \tilde{t}} = 0, \tag{60}$$

thus yields the Ruina (1983) stability condition [3].

QSSA validity conditions

A necessary aspect of the QSSA is that the duration of the pre-steady-state period is much shorter than the characterstic time for the pore pressure evolution. An essential condition for the QSSA to be valid after the pre-steady state is therefore $t_\Theta \ll t_\mathrm{P}$,

$$0 < c = \left(\frac{d_\mathrm{c}}{V_0}\right) \Big/ \left(\frac{\eta L}{k_\mathrm{n}^\mathrm{eff} k}\right) \ll 1. \tag{61}$$

Note that the initial condition $P(0) = P_0$ is reasonable for the QSSA only if there is a negligible relative change $|\Delta P/P_0|$ in pore pressure during the pre-steady state. We

estimate $|\Delta P/P_0|$ by

$$\left|\frac{\Delta P}{P_0}\right| \approx \frac{1}{P_0}\left|\frac{\partial P}{\partial t}\right|_{\max} t_\Theta. \tag{62}$$

An additional condition for the validity of the QSSA is therefore

$$0 < rq = \frac{d_c k_n^{\text{eff}}}{V_0}\frac{Q}{P_0} \ll 1. \tag{63}$$

Recall that parameter c is the normalized diffusivity or ratio of the pore pressure to the state evolution timescales and parameter rq is the normalized injection rate, where $r = t_\Theta k_n^{\text{eff}}$ and $q = Q/P_0$.

Error estimates

This analysis shows that using the QSSA to study the stability of steady frictional sliding to small perturbations in velocity with an evolving pore pressure is justified when conditions Eqs. (61) and (63) are met. In other words, if in a timescale t_Θ sliding reaches steady state with a constant pore pressure, then assuming that sliding is in a quasi-steady state with a changing pore pressure is valid when the pore pressure change occurs on a time scale t_P that is long compared to t_Θ and $\Delta P|_{t_\Theta}$ is small compared to P_0.

Therefore, we expect that the accuracy of our instability criterion depends on dimensionless parameters c and rq. Here we evaluate the error in the analytical estimate of the critical stiffness required to trigger the first slip event (Supplementary Figure 4). We indeed find that the error decreases as c or rq decrease. It becomes small ($< 15\%$) when the normalized diffusivity and normalized injection rate reach small values ($c \leq 5 \times 10^{-2},\ rq \leq 5 \times 10^{-3}$). It is also interesting to note that the QSSA validity may be extended to instances where c is of order one provided that rq is significantly smaller than one (green curve).

Supplementary Note 7

Application to the Denver earthquakes

To bridge the gap between the analysis of the idealized spring-poroslider model and the real world, we express our instability criterion in dimensional form, and identify values of dimensionless parameters c and rq that correspond to real-world settings.

In dimensional form, the critical stiffness from the linear stability analysis is

$$k_{\mathrm{s,crit}} = \frac{(\hat{b}-\hat{a})}{d_{\mathrm{c}}}(\Sigma - P) + \frac{\hat{\alpha}}{V_0}\dot{P}, \tag{64}$$

or, equivalently,

$$k_{\mathrm{s,crit}} = \left[(\hat{b}-\hat{a}) + \hat{\alpha}\frac{d_{\mathrm{c}}}{V_0}\frac{\dot{P}}{(\Sigma - P)}\right]\frac{(\Sigma - P)}{d_{\mathrm{c}}}, \tag{65}$$

where the term $\hat{b}-\hat{a}$ represents the original velocity weakening effect and the dimensionless term $\hat{\alpha}(d_{\mathrm{c}}/V_0)\dot{P}/(\Sigma - P)$ represents an additional weakening effect from fluid pressurization. Note that this pressurization term is maximum at early times and is approximately equal to rq.

The 1960s Denver earthquakes is a good example of a real-world setting, where it is well-documented that injection of wastewater into the fractured Precambrian granite gneiss underneath the Rocky Mountain Arsenal triggered the earthquakes and where injection rate is directly related to the frequency of earthquakes [19, 20]. The reservoir spans a depth interval from 3.7 to 7 km below the surface. Experimental data on granite at this depth shows velocity weakening behavior ($\hat{b}-\hat{a}$ in the range 0.002 to 0.005, $\mu_0 = 0.7$ to 0.75) [21].

To identify values of dimensionless parameter c that correspond to this setting, we estimate the state evolution timescale t_Θ and the pore pressure evolution timescale t_{p}:

$$c = \frac{t_\Theta}{t_{\mathrm{P}}}. \tag{66}$$

The state evolution timescale t_Θ is

$$t_\Theta = \frac{d_c}{V_0}. \tag{67}$$

We find that t_Θ ranges from 10 days to 4 months based on field data of the characteristic slip distance and loading rate ($d_\mathrm{c} = 10^{-3}$ to 10^{-2} m, $V_0 = 10^{-9}$ m s^{-1}) [22, 4].

The pore pressure evolution time scale t_P can be transferred from the poroslider model to field settings,

$$t_\mathrm{P} = \underbrace{\frac{\eta L}{k_\mathrm{n}^\mathrm{eff} k}}_{\text{poroslider}} = \frac{L}{k/\eta}\left[\frac{1}{k_\mathrm{n}} + H_0 c_\mathrm{f}\right] = \frac{L^2}{k/\eta}\left[\frac{1}{K_\mathrm{v}} + \phi\frac{1}{K_\mathrm{f}}\right] = \frac{L^2}{k/\eta}\frac{S_\mathrm{s}}{\rho g} = \underbrace{\frac{L^2 S}{T}}_{\text{field}}. \tag{68}$$

We find that t_P is approximately 2 years based on a reservoir analysis of the Denver earthquakes, with transmissivity $T = 10^{-5}$ m^2 s^{-1}, storativity $S = 10^{-5}$, and characteristic length scale $L = 8 \times 10^3$ m [23].

In a similar manner, we identify values of dimensionless parameter rq. We translate this quantity from the poroslider model to field settings:

$$rq = \underbrace{\frac{d_\mathrm{c}}{V_0} k_\mathrm{n}^\mathrm{eff} \frac{Q}{P_0}}_{\text{poroslider}} = \frac{d_\mathrm{c}}{V_0} k_\mathrm{n}^\mathrm{eff} \frac{Q_\mathrm{w}}{P_0 W B} = \frac{d_\mathrm{c}}{V_0} \frac{\left[\frac{1}{K_\mathrm{v}} + \phi\frac{1}{K_\mathrm{f}}\right]^{-1}}{L} \frac{Q_\mathrm{w}}{P_0 W B} = \underbrace{\frac{d_\mathrm{c}}{V_0} \frac{\rho g}{LS} \frac{Q_\mathrm{w}}{P_0 W}}_{\text{field}}, \tag{69}$$

and evaluate values based on the reservoir analysis and injection data, with reservoir pressure $P_0 = 30$ MPa, reservoir width $W = 3 \times 10^3$ m, and field injection rate $Q_\mathrm{w} = 2$ to 9 million gal mo^{-1} [19, 23].

Therefore, reasonable estimates of c and rq for this setting would be in the order of 10^{-2} to 10^{-1} and 10^{-3} to 10^{-1}, respectively. Note that both estimates are much smaller than one, and thus meet the QSSA validity conditions (Supplementary Figure 5).

Having determined the validity of the QSSA analysis to this setting, we now assess whether pressurization rate effects were likely significant during fluid injection leading

to the Denver earthquakes. In dimensionless form, the critical stiffness κ_{crit} is given by Eq. (S29). Prior to fluid injection, the pore pressure is constant and the critical stiffness,

$$\kappa_{\text{crit}} = (b-a)(\sigma - p_0), \tag{70}$$

is estimated to be 0.005 ($b-a = 0.003$ to 0.007, $\sigma - p_0 = 1$). Shortly following the start of fluid injection, the pore pressure increases rapidly and the dimensionless critical stiffness takes the form:

$$\kappa_{\text{crit}}\Big|_{t=0} = (b-a)(\sigma - p_0) + \frac{\alpha}{v_0}\dot{p}\Big|_{t=0} = (b-a)(\sigma - p_0) + \frac{\alpha}{v_0} rq. \tag{71}$$

This results in an increase in critical stiffness at early times of around 300% ($\alpha = 1$, $v_0 = 1$, $b - a = 0.005$, $rq = 10^{-2}$), thus indicating that the additional weakening effect from fluid pressurization is likely significant in this setting.

Supplementary Note 8

Phase diagram of injection-induced seismicity

To study the influence of reservoir properties on injection-induced seismicity, we simulate the occurrence of earthquakes as a function of dimensionless injection rate $rq = d_c k_n^{eff} Q/(p_c V_*)$ and normalized diffusivity $c = d_c k_n^{eff} k/(\eta L V_*)$ for the case $a = 0$, $b = 0.01$, $\alpha = 1$, and $\kappa = 0.011$ (Supplementary Figure 6). Diffusivity is varied by varying permeability. Each point on the phase diagram represents the maximum slip velocity of a different simulation run with a particular injection rate and a particular normalized diffusivity. The red dots indicate the occurrence of one or more earthquakes over a finite time period, whereas the grey dots indicate the absence of earthquakes over the same period. We observe two distinct regimes depending on the normalized diffusivity: a high diffusivity regime for $c > 1$, and a low diffusivity regime for $c < 0.01$.

When the normalized diffusivity is higher than one, the dimensionless pressure diffusion time is less than one. Pore pressure reaches steady-state on a very short time scale, and so the rate of change in pore pressure is negligible. To quantify this, we write

$$\dot{p} \approx 0, \tag{72}$$

$$p \approx p_0 + \frac{rq}{c}. \tag{73}$$

It is helpful to express the condition for instability (Eq. (29)) in terms of rq_{crit} so that an earthquake is triggered if the injection rate is higher than a critical value given by

$$rq_{crit} \approx \left[(\sigma - p_0) - \frac{\kappa}{(b-a)}\right] c. \tag{74}$$

We find that the injection rate required to trigger an earthquake is proportional to diffusivity c, which explains the simulation results in Supplementary Figure 6: In the regime of high diffusivity $c > 1$, $q_{crit} \sim c$. Accordingly, earthquakes are more easily triggered

when fluid is injected into a low permeability reservoir rock than a high permeability, for a fixed effective stiffness.

Conversely, when the normalized diffusivity is lower than 0.001, the dimensionless pressure diffusion time is more than 100. Pore pressure stays near the initial transient-state throughout the simulation period and so the magnitude of change in pore pressure is negligible. To quantify this, we write

$$\dot{p} \approx rq, \tag{75}$$

$$p \approx p_0. \tag{76}$$

If we express the condition for instability in terms of rq_{crit}, similar to the high diffusivity case above, we find that the injection rate required to trigger an earthquake is

$$rq_{\mathrm{crit}} \approx \frac{v_0}{\alpha}\Big[\kappa - (b-a)(\sigma - p_0)\Big]. \tag{77}$$

This also explains the simulation results in Supplementary Figure 6: In the regime of low diffusivity $c < 0.01$, $q_{\mathrm{crit}} \sim$ const. Accordingly, in this regime, earthquake triggering is independent of permeability. These results, as a whole, suggest that reservoirs with high hydraulic diffusivity and low stiffness may be safer sites for fluid injection operations compared to sites with low hydraulic diffusivity and high stiffness.

Supplementary Note 9

Earthquake likelihood vs. injection duration

Supplementary Figure 7 shows the likelihood of earthquakes as a function of the duration of the injection period for a fixed total injected volume. As can be seen, the earthquake likelihood, inferred from the peak critical stiffness, is strongly dependent on the duration of injection. A shorter injection duration or, equivalently, a higher injection rate results in a higher likelihood of earthquake triggering.

Supplementary Figures

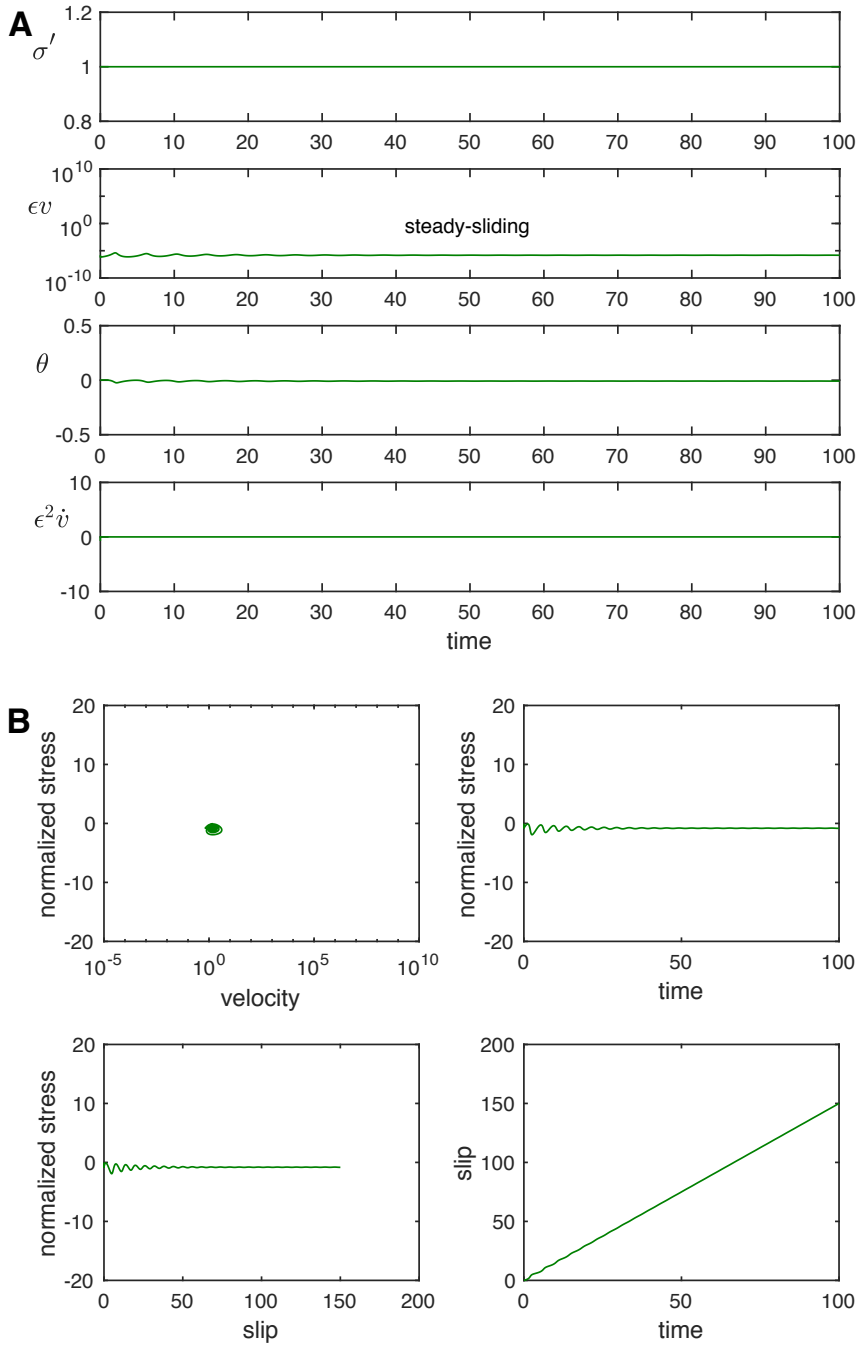

Supplementary Figure 1: Dynamics of the spring-poroslider system without fluid injection, for velocity-weakening friction. Top figure (A) shows time evolution of normal effective stress $(\sigma - p)$, velocity ϵv, state variable θ, and magnitude of the inertia term $\epsilon \dot{v}$. Bottom figure (B) shows plots of normalized stress as a function of velocity, time, and slip. Red curves represent the slip phase, blue curves represent the stick phase, and green curves represent steady-sliding.

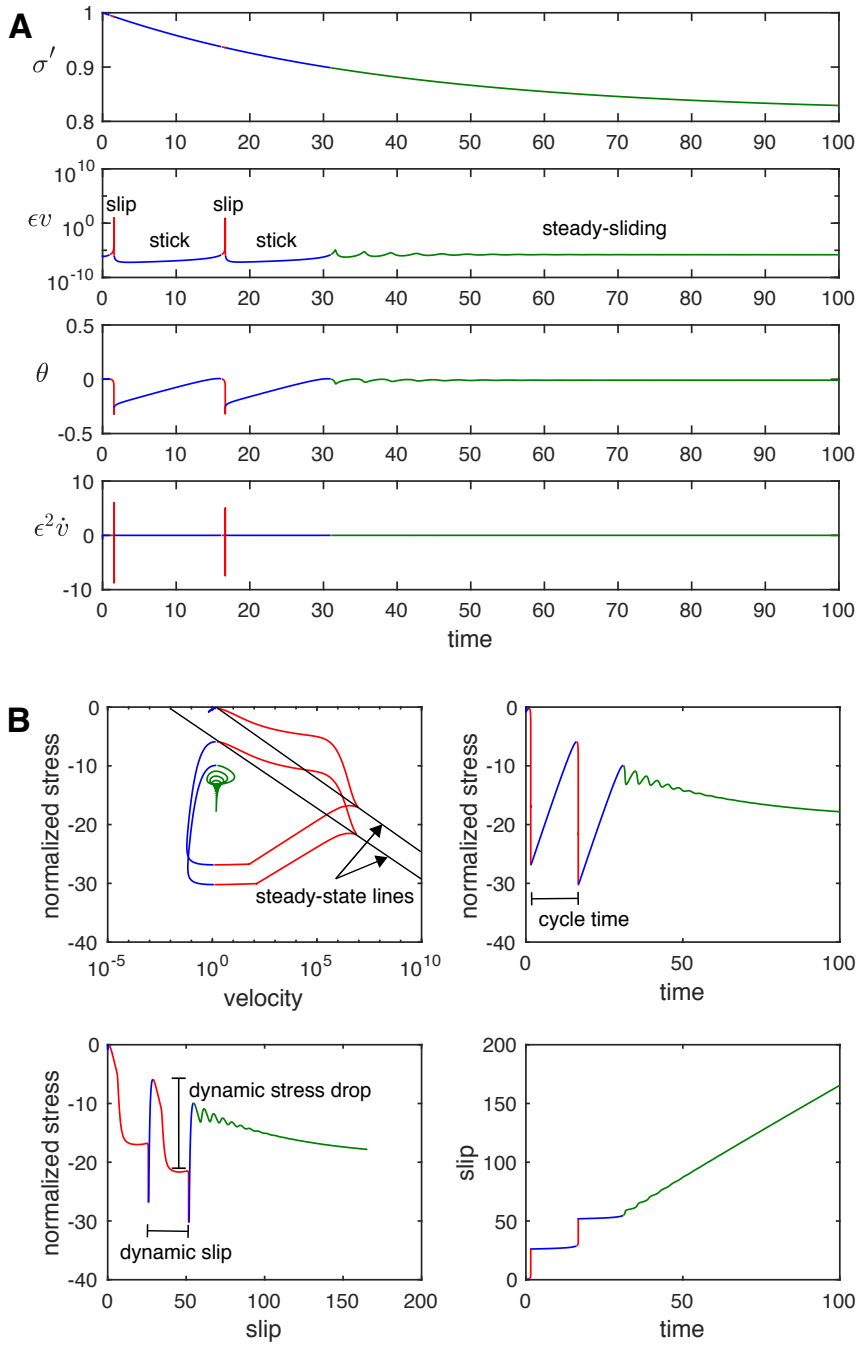

Supplementary Figure 2: Dynamics of the spring-poroslider system under constant fluid injection rate, for velocity-weakening friction. Top figure (A) shows time evolution of normal effective stress $(\sigma - p)$, velocity ϵv, state variable θ, and magnitude of the inertia term $\epsilon \dot{v}$. Bottom figure (B) shows plots of normalized stress as a function of velocity, time, and slip. Red curves represent the slip phase, blue curves represent the stick phase, and green curves represent steady-sliding.

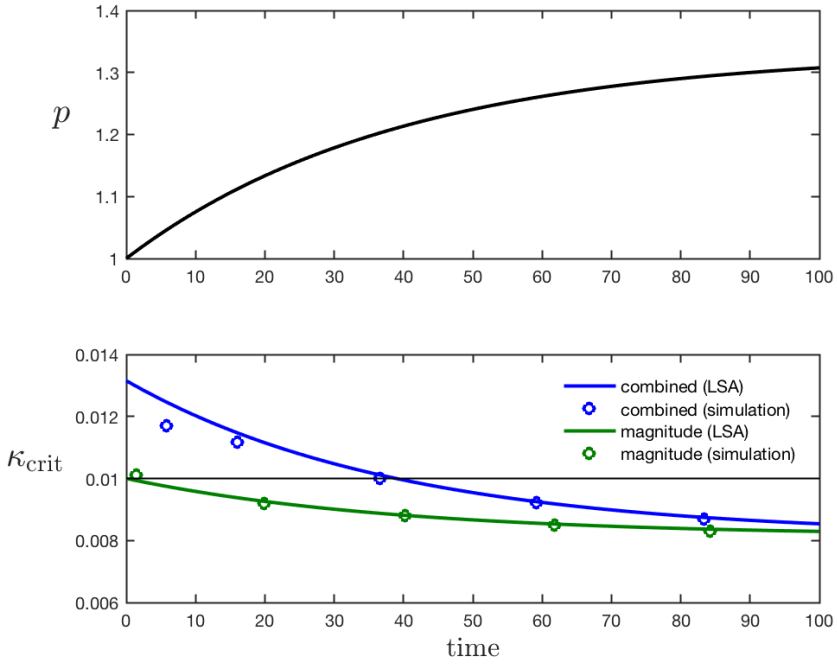

Supplementary Figure 3: Analytical vs. numerical estimates of critical stiffness κ_{crit} for a case with normalized diffusivity of $c = 3 \times 10^{-2}$ and normalized injection rate of $rq = 5 \times 10^{-3}$. Solid line represents the analytical estimate, and open circles represent numerical ones. Blue represents the combined rate and magnitude effect (setting $\alpha = 1$), and green represents the magnitude effect (setting $\alpha = 0$). The black horizontal line represents κ_{crit} prior to fluid injection.

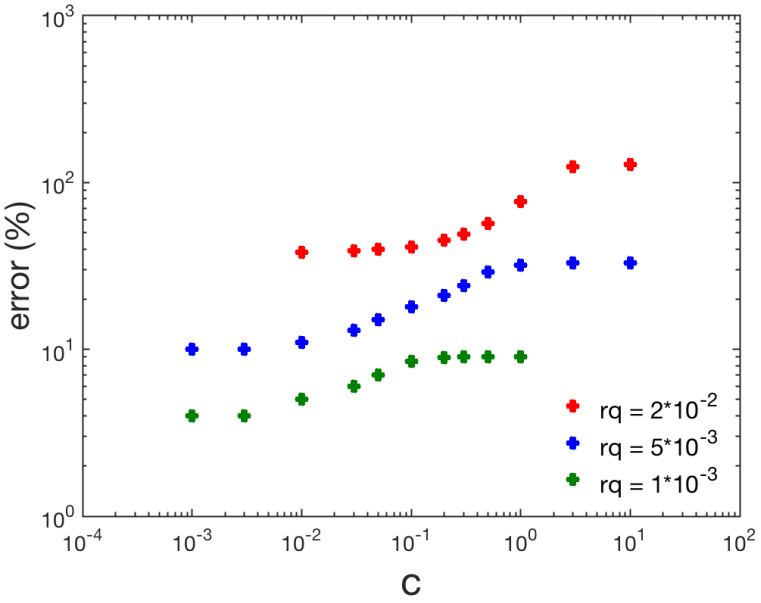

Supplementary Figure 4: Error in the instability criterion as a function of c and rq. The error is taken as the ratio of the maximum difference between the analytical and numerical estimates of the critical stiffness required to trigger the first slip event to the numerical estimate. The dimensionless parameter c is varied by varying permeability k, and rq is varied by varying injection rate Q.

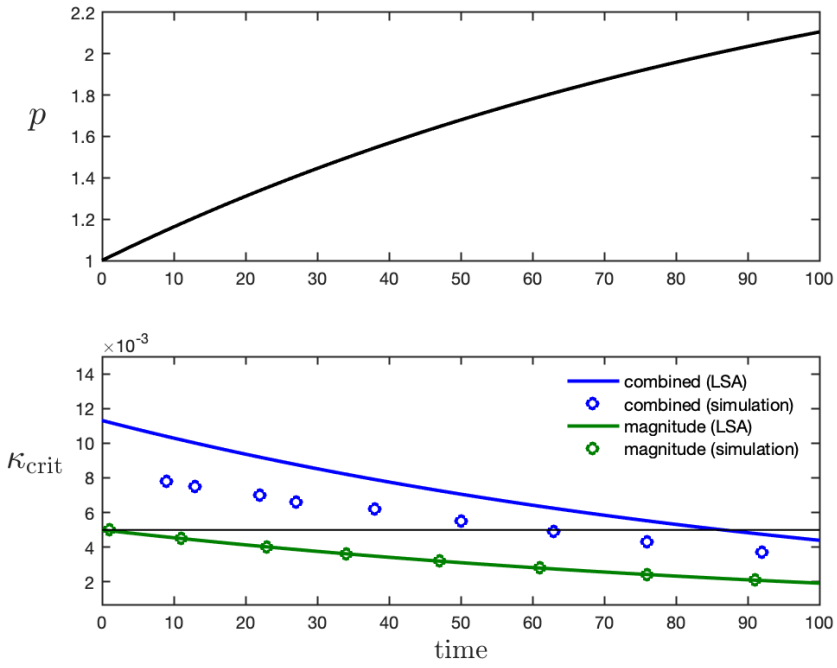

Supplementary Figure 5: Analytical vs. numerical estimates of critical stiffness κ_{crit} for a case with normalized diffusivity of $c = 1 \times 10^{-2}$ and normalized injection rate of $rq = 1 \times 10^{-2}$. Solid line represents the analytical estimate, and open circles represent numerical ones. Blue represents the combined rate and magnitude effect (setting $\alpha = 1$), and green represents the magnitude effect (setting $\alpha = 0$). The black horizontal line represents κ_{crit} prior to fluid injection.

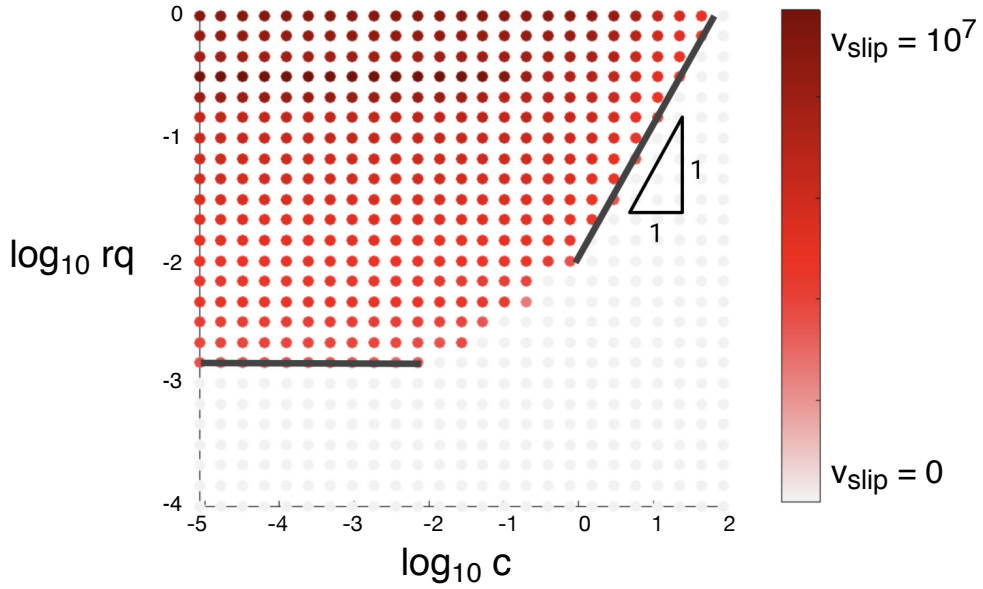

Supplementary Figure 6: Phase diagram of triggered earthquakes as a function of dimensionless injection rate rq and normalized diffusivity c. Diffusivity is varied by varying permeability k. The dots show the maximum slip rate in log scale, where red represents occurrence of one or more earthquakes during a finite simulation period, and grey represents the absence of earthquakes over the same time period.

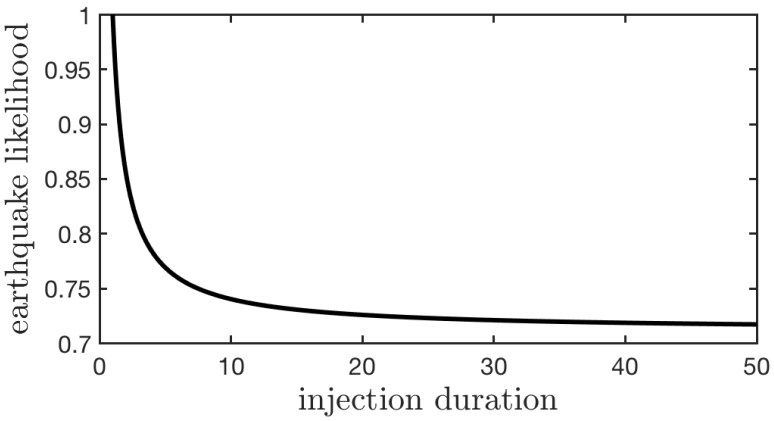

Supplementary Figure 7: Earthquake likelihood vs. injection duration. The earthquake likelihood is computed as a normalized initial critical stiffness for a given injection duration ($\kappa_{\mathrm{crit}}|_{\mathrm{T}}/\kappa_{\mathrm{crit}}|_{\mathrm{T_{min}}}$). The injection duration is computed as the ratio of a fixed total injection volume to the injection rate ($T = V/q$).

Supplementary References

1. Dieterich, J. H. Modeling of rock friction: 1. Experimental results and constitutive equations. *Journal of Geophysical Research: Solid Earth* **84**, 2161–2168 (1979).

2. Dieterich, J. H. Modeling of rock friction: 2. Simulation of preseismic slip. *Journal of Geophysical Research: Solid Earth* **84**, 2169–2175 (1979).

3. Ruina, A. Slip instability and state variable friction laws. *Journal of Geophysical Research: Solid Earth* **88**, 10359–10370 (1983).

4. Marone, C. Laboratory-derived friction laws and their application to seismic faulting. *Annual Review of Earth and Planetary Sciences* **26**, 643–696 (1998).

5. Linker, M. & Dieterich, J. H. Effects of variable normal stress on rock friction: Observations and constitutive equations. *Journal of Geophysical Research: Solid Earth* **97**, 4923–4940 (1992).

6. Richardson, E. & Marone, C. Effects of normal stress vibrations on frictional healing. *Journal of Geophysical Research: Solid Earth* **104**, 28859–28878 (1999).

7. Olsson, W. A. The effects of normal stress history on rock friction. In *The 29th US Symposium on Rock Mechanics*, 111–117 (American Rock Mechanics Association, 1988).

8. Wang, W. & Scholz, C. Micromechanics of the velocity and normal stress dependence of rock friction. *Pure and Applied Geophysics* **143**, 303–315 (1994).

9. Kilgore, B., Lozos, J., Beeler, N. & Oglesby, D. Laboratory observations of fault strength in response to changes in normal stress. *Journal of Applied Mechanics* **79**, 031007 (2012).

10. Perfettini, H., Schmittbuhl, J., Rice, J. R. & Cocco, M. Frictional response induced by time-dependent fluctuations of the normal loading. *Journal of Geophysical Research: Solid Earth* **106**, 13455–13472 (2001).

11. Hong, T. & Marone, C. Effects of normal stress perturbations on the frictional properties of simulated faults. *Geochemistry, Geophysics, Geosystems* **6**, Q03012 (2005).

12. Rice, J. R. & Tse, S. T. Dynamic motion of a single degree of freedom system following a rate and state dependent friction law. *Journal of Geophysical Research: Solid Earth* **91**, 521–530 (1986).

13. Wang, H. F. *Theory of linear poroelasticity with applications to geomechanics and hydrogeology* (Princeton University Press, 2000).

14. Lick, W. The instability of a fluid layer with time-dependent heating. *Journal of Fluid Mechanics* **21**, 565–576 (1965).

15. Robinson, J. Theoretical analysis of convective instability of a growing horizontal thermal boundary layer. *The Physics of Fluids* **19**, 778–791 (1976).

16. Segel, L. A. & Slemrod, M. The quasi-steady-state assumption: a case study in perturbation. *SIAM Review* **31**, 446–477 (1989).

17. Rao, C. V. & Arkin, A. P. Stochastic chemical kinetics and the quasi-steady-state assumption: Application to the Gillespie algorithm. *The Journal of Chemical Physics* **118**, 4999–5010 (2003).

18. Lin, C.-C. & Segel, L. A. *Mathematics applied to deterministic problems in the natural sciences* (SIAM, 1988).

19. Evans, D. M. The Denver area earthquakes and the Rocky Mountain Arsenal disposal well. *The Mountain Geologist* **3**, 23–36 (1966).

20. Healy, J., Rubey, W., Griggs, D. & Raleigh, C. The Denver earthquakes. *Science* **161**, 1301–1310 (1968).

21. Blanpied, M., Lockner, D. & Byerlee, J. Fault stability inferred from granite sliding experiments at hydrothermal conditions. *Geophysical Research Letters* **18**, 609–612 (1991).

22. Scholz, C. The critical slip distance for seismic faulting. *Nature* **336**, 761 (1988).

23. Hsieh, P. A. & Bredehoeft, J. D. A reservoir analysis of the Denver earthquakes: A case of induced seismicity. *Journal of Geophysical Research: Solid Earth* **86**, 903–920 (1981).